



HAL
open science

Upgrades to the MAVEN Echelle Data Reduction Pipeline: New Calibration Standard and Improved Faint Emission Detection Algorithm at Lyman- α

M. Mayyasi, J. Clarke, Jean-Loup Bertaux, J. Deighan, D. Bhattacharyya, M. Chaffin, S. Jain, N. Schneider, S. Curry

► **To cite this version:**

M. Mayyasi, J. Clarke, Jean-Loup Bertaux, J. Deighan, D. Bhattacharyya, et al.. Upgrades to the MAVEN Echelle Data Reduction Pipeline: New Calibration Standard and Improved Faint Emission Detection Algorithm at Lyman- α . *Earth and Space Science*, 2023, 10 (4), pp.e2022EA002602. 10.1029/2022ea002602 . insu-03911930v2

HAL Id: insu-03911930

<https://insu.hal.science/insu-03911930v2>

Submitted on 27 Apr 2023

HAL is a multi-disciplinary open access archive for the deposit and dissemination of scientific research documents, whether they are published or not. The documents may come from teaching and research institutions in France or abroad, or from public or private research centers.

L'archive ouverte pluridisciplinaire **HAL**, est destinée au dépôt et à la diffusion de documents scientifiques de niveau recherche, publiés ou non, émanant des établissements d'enseignement et de recherche français ou étrangers, des laboratoires publics ou privés.



Distributed under a Creative Commons Attribution 4.0 International License

Earth and Space Science



METHOD

10.1029/2022EA002602

Key Points:

- MAVEN/ECH uses HST/STIS, the only other UV echelle instrument deployed to space, for calibration and independent verification
- The MAVEN/ECH data reduction algorithm has been upgraded to improve detection of faint D Lyman- α emissions
- The scientific implications of this work include doubling the previous data set of D measurements available for reliable interpretation

Correspondence to:

M. Mayyasi,
majdm@bu.edu

Citation:

Mayyasi, M., Clarke, J., Bertaux, J.-L., Deighan, J., Bhattacharyya, D., Chaffin, M., et al. (2023). Upgrades to the MAVEN Echelle data reduction pipeline: New calibration standard and improved faint emission detection algorithm at Lyman- α . *Earth and Space Science*, 10, e2022EA002602. <https://doi.org/10.1029/2022EA002602>

Received 7 SEP 2022

Accepted 7 DEC 2022









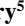
Author Contributions:

Conceptualization: M. Mayyasi
Data curation: M. Mayyasi, J. Deighan, D. Bhattacharyya, S. Jain
Formal analysis: M. Mayyasi
Investigation: M. Mayyasi
Methodology: M. Mayyasi, J. Clarke, J.-L. Bertaux
Project Administration: S. Curry
Resources: M. Mayyasi
Software: M. Mayyasi
Validation: M. Mayyasi, J.-L. Bertaux
Visualization: M. Mayyasi
Writing – original draft: M. Mayyasi

© 2022 The Authors. Earth and Space Science published by Wiley Periodicals LLC on behalf of American Geophysical Union.

This is an open access article under the terms of the [Creative Commons Attribution-NonCommercial-NoDerivs License](https://creativecommons.org/licenses/by-nc-nd/4.0/), which permits use and distribution in any medium, provided the original work is properly cited, the use is non-commercial and no modifications or adaptations are made.

Upgrades to the MAVEN Echelle Data Reduction Pipeline: New Calibration Standard and Improved Faint Emission Detection Algorithm at Lyman- α

M. Mayyasi¹ , J. Clarke² , J.-L. Bertaux³ , J. Deighan⁴ , D. Bhattacharyya⁴ , M. Chaffin⁴ , S. Jain⁴ , N. Schneider⁴ , and S. Curry⁵ 

¹Center for Space Physics, Boston University, Boston, MA, USA, ²Astronomy Department, Boston University, Boston, MA, USA, ³LATMOS/IPSL, Guyancourt, France, ⁴Laboratory for Atmospheric and Space Physics, UC Boulder, Boulder, CO, USA, ⁵Space Sciences Laboratory, University of California, Berkeley, CA, USA

Abstract The Mars Atmosphere and Volatile Evolution (MAVEN) mission instrument suite includes an ultraviolet echelle spectrograph with high-spectral resolution designed to resolve D and H Lyman- α emissions. The high-spectral resolution mode was previously characterized in the lab and in the cruise phase to Mars and had been calibrated using observations and models of interplanetary hydrogen Lyman- α emissions. This work presents improved characterizations of the high-spectral resolution mode using in-orbit observations that allow for more robust detections of the faint D Lyman- α emission line. Additionally, the instrument was re-calibrated using simultaneous and comparable observations made with the Hubble Space Telescope high-spectral resolution instrument. Comparisons to Lyman- α observations made with the low-resolution UV channel on the spectrometer, that had been calibrated with stars, showed consistency in the brightness values for measurements obtained at similar observational conditions. The combined upgrades to the faint-emission fitting and new calibration techniques of the MAVEN echelle channel have resulted in an improved data-reduction pipeline with favorable implications for the science utility of D and H Lyman- α emissions.

Plain Language Summary The MAVEN high resolution echelle (ECH) instrument has been used to observe ultraviolet emissions from Mars. Measurements made with MAVEN/ECH were made available to the public by using a data reduction pipeline that had been developed with in-lab and theoretical analysis to convert observations into a form that was useable by the broader scientific community. Since MAVEN's orbit insertion in 2014, the ECH detector has been better characterized with lessons learned from in-orbit performance. These improvements produced a new data reduction pipeline that has enhanced the detection of faint D Lyman- α emissions that are critical to interpreting water loss from the upper atmosphere of Mars.

1. Introduction

The MAVEN mission launched in November 2013 and arrived at Mars in September 2014. MAVEN has since been orbiting the planet in an elliptical near-polar orbit, making routine observations of the atmosphere with in-situ measurements as well as with remote sensing techniques (Jakosky et al., 2015).

One of the remote sensing instruments on board MAVEN is the Imaging Ultraviolet Spectrograph (IUVS) that is designed to measure UV emissions of planetary species. The IUVS instrument operates in three observation modes: (a) MUV, observing in the mid-ultraviolet range of 180–330 nm with low spectral resolution of 1.2 nm; (b) FUV, observing in the far ultraviolet range of 115–190 nm with low-spectral resolution of 0.6 nm; and (c) Echelle, observing in the far ultraviolet range of 116–131 nm, with high spectral resolution $R \sim 17,000$ (McClintock et al., 2014). The low spectral resolution modes were calibrated with stars (Chaffin et al., 2018). Both the high- and low-spectral resolution modes have been checked for consistency and calibrated using the Solar and Heliospheric Observatory (SOHO) mission's Solar Wind Anisotropy (SWAN) instrument (Mayyasi, Clarke, Quémerais, et al., 2017).

Since early mission calibration, the SWAN instrument has shown some degradation that motivated re-calibrating the MAVEN IUVS Echelle channel with another source. The Hubble Space Telescope (HST) mission's Space Telescope Imaging Spectrograph (STIS) is an ideal candidate for use as a calibration standard as it is robust

Writing – review & editing: M. Mayyasi, J. Clarke, J.-L. Bertaux, D. Bhattacharyya, M. Chaffin, N. Schneider

(Bohlin et al., 2019) and utilizes observation modes that have similar spectral resolution to the MAVEN Echelle instrument (Sohn et al., 2019).

Additional insights into the MAVEN Echelle mode optical characteristics and performance, obtained since early mission, include improved determinations of the instrument line spread function, in-orbit characterizations of the detector, and a clearer understanding of the instrument background level. The lessons learned from science-phase mission observations as well as the need to obtain an alternative standard for calibration motivated an upgrade to the Echelle data reduction pipeline. This work describes these updates as well as their implications for doing science with the MAVEN IUVS Echelle channel.

2. Observations and Instruments

Hydrogen (H) and Deuterium (D) atoms resonantly scatter ultraviolet (UV) photons at Lyman- α wavelengths. The high-spectral resolution (Echelle) mode of the IUVS detector is designed to allow for the spectral separation and detection of these atmospheric H and D Lyman- α emissions at 121.567 and 121.534 nm, respectively (McClintock et al., 2014). Mars planetary emissions can extend several Martian radii around the planet and can engulf orbiting spacecraft (e.g., Anderson & Hord, 1971; Bertaux et al., 2006; Chaffin et al., 2015; Chamberlain, 1963). Observations made by MAVEN/IUVS are either pointed at or away from the planetary disk. When the IUVS instrument line of sight is pointed off the disk of Mars, with pointing ranging from the limb of the planetary disk to diametrically opposite to the planet, atmospheric emissions along portions of the line of sight include varying contributions from thermal H and D, non-thermal H and D, and interplanetary H atoms. Such multi-sourced emissions result in spectra that compound the effects of different populations of H atoms at Lyman- α and would not be suited for quantifying the instrument detector response to single-emission thermal planetary populations. Therefore, to minimize the effects of exogenic emission properties on the instrument characterization, IUVS and HST disk-pointed observations were used. The high spectral resolution echelle mode was adopted to spectrally resolve, isolate, and quantify individual D and H Lyman- α emissions.

During an observing campaign in November 2018, HST was successfully used to obtain spatially resolved spectra of the disk of Mars with STIS at a time that overlapped with MAVEN/IUVS Echelle on-disk observations. Given the similar spectral resolution at Lyman- α of the echelle spectrograph of each instrument, these overlapping observations were utilized for cross-calibration. HST Lyman- α observations of Mars are made from Low Earth Orbit and therefore can include contributions from H emissions in the geocorona, the interplanetary medium, and Mars. The abundance of D atoms falls off more rapidly with thermospheric altitudes than H atoms, resulting in negligible contamination of the HST/STIS terrestrial D Lyman- α signal along the line of sight to Mars (Ben Jaffel et al., 2007; Chaufray et al., 2010; Clarke et al., 2004, 2019; Quémerais et al., 2006, 2009).

The D Lyman- α emissions at Mars are typically faint (typically a few tens to hundreds of Rayleigh) compared with H Lyman- α emissions (typically several kilo-Rayleigh), and both have shown seasonal variability (Bhattacharyya et al., 2015; Chaffin et al., 2014; Clarke et al., 2014; Mayyasi, Clarke, Bhattacharyya, et al., 2017). During Mars' perihelion season, D emissions are brightest and therefore most ideal for spectral observing (Mayyasi et al., 2019). The HST observing campaign utilized for this work was scheduled at a time when Mars was near perihelion (on 16 September 2018), so that D emissions could be used instead of H emissions for the cross-calibration efforts in this work. Table 1 lists the observational details of each instrument data set and Figure 1 shows the HST and IUVS lines of sight.

3. Method

Early in the MAVEN mission, the IUVS instrument Echelle data reduction pipeline included preliminary characterizations of the detector using in-lab and in-cruise observations. Since orbit insertion, experimental optical settings have stabilized, and a significant number of on-disk observations have been made to facilitate improved characterization of the IUVS Echelle detector. Incorporating lessons learned from several years in orbit, the data reduction pipeline has been upgraded to include a more accurate background level mitigation technique, an updated and empirically derived line spread function, and a robust integration process that accounts for multiple binning schemes, voltage settings, and that accommodates the new line spread function. These improvements result in more accurate detections of faint emissions and improved assessments of measurement uncertainties pertaining to detector background. Recalibration of MAVEN/IUVS with HST/STIS using the disk of Mars as the

Table 1
Observational Conditions of Each of the HST/STIS and the MAVEN/IUVS Echelle Calibration Measurements

Date (Ls), MY	November 8–9, 2018 (Ls = 284°), Mars Year 34	
Spacecraft	HST	MAVEN
Mode	STIS, 52 × 0.5 E140H	Echelle
Orbit(s)	odti04weq (DOY 312)	8010, 8014, 8018
UTC	22:23:09.0	Orbit 8010: 2018/312 November 08 01:49:05.60713 → 02:02:35.60775 Orbit 8014: 2018/312 November 08 19:24:46.01723 → 19:38:16.01785 Orbit 8018: 2018/313 November 09 13:00:23.68970 → 13:13:53.69032
SZA	0°–70°	~82°
LAT	65°S–11°N	~60°–5°S

Note. Ls, solar longitude; DOY, Day of Year; SZA, solar zenith angle along the line of sight; and LAT, Martian latitude along the line of sight. For HST, a subset of the data was selected where the line of sight was pointed at the planetary disk. The geometry is derived for the point where the line of sight intersects the planetary disk.

calibration standard is a key component of the data reduction pipeline upgrade and is included in this work. The individual updates are described in more detail below.

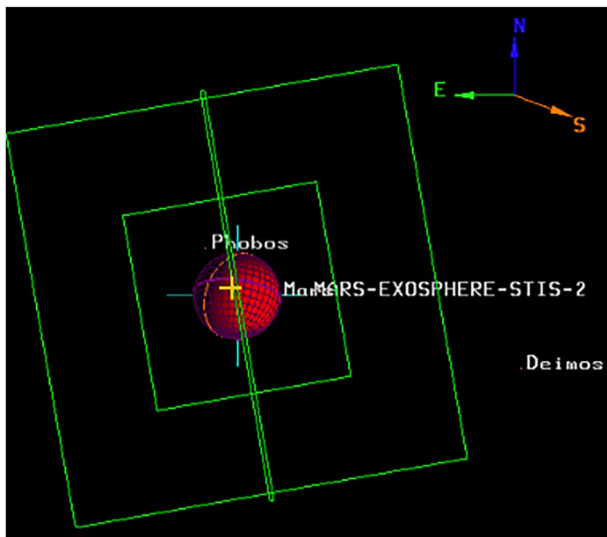


Figure 1. The observational configuration for Mars (red shaded disk) obtained from the HST Phase II target confirmation chart for the calibration data used in this work. The large green box denotes the full 50'' × 50'' field of view of the CCD detector for a broad wavelength range. The inner green box denotes the 25'' × 25'' field of view of the HST/STIS MAMA detector used in this work. The narrow green rectangle denotes the 52'' × 0.5'' HST/STIS aperture. The pale blue cross is the center of the HST/STIS FOV and is centered on the disk of Mars. The purple arc denotes the planetary equator, and the orange arc represents the terminator line. The axes on the top right indicate the location of the Sun (S), terrestrial North (N) and terrestrial East (E). Labels for the Martian moons are indicated next to the orange dots of their location in the observation. The labels for Mars and Mars-Exosphere-STIS-2 (assigned by the observer during Phase II planning) are indicated. The orange cross indicates the location of the MAVEN/IUVS/ECH line of sight for the simultaneous observations utilized for cross-calibration.

3.1. Binning Schemes

The IUVS detectors on MAVEN/IUVS are 1024 × 1024 pixels. Subsets of the full detector are used for data download, and these are binned in variable ways to optimize science utility of various types of observations (Mayyasi, Clarke, Quémerais, et al., 2017). In the region on the detector where the Lyman- α photons are projected, binning of the detector pixels along the spectral dimension has remained consistent throughout most binning schemes. However, binning along the spatial dimension has varied considerably. A subset of early mission binning schemes (described in Table A1 in Mayyasi, Clarke, Quémerais, et al., 2017 as 201 × 287 and 1024 × 1024) have been expanded to include: 201 × 18, 160 × 50, 160 × 159, 512 × 92, 386 × 64, and 332 × 74 where the format represents the number of spectral bins × the number of spatial bins. The number of spectral and spatial bins have varied throughout the mission, and sample different regions on the detector, but the resolution of the spectral bins has remained fixed. The only un-binned (full spectral resolution across the entire detector) observations made with the MAVEN/IUVS echelle mode were obtained early in the mission for diagnostic purposes and are limited. In these full-frame observations, the wavelength resolution, $d\lambda$ is 0.00071 nm. For all other observations, the spectral range has been consistently binned ×2, resulting in a wavelength resolution, $d\lambda$ of 0.00143 nm. The upgraded data reduction pipeline includes spatial integration across the full aperture at the Lyman- α signal region that spans a consistent region of the detector across all existing binning schemes.

3.2. Background Mitigation

The background counts in the IUVS echelle spectral images are due to a combination of scattered Lyman- α emissions and charged particle background in the detector. In both these cases the background is not uniform across the detector, and it changes with time, requiring independent derivation for each image. In the previous data reduction pipeline, the background

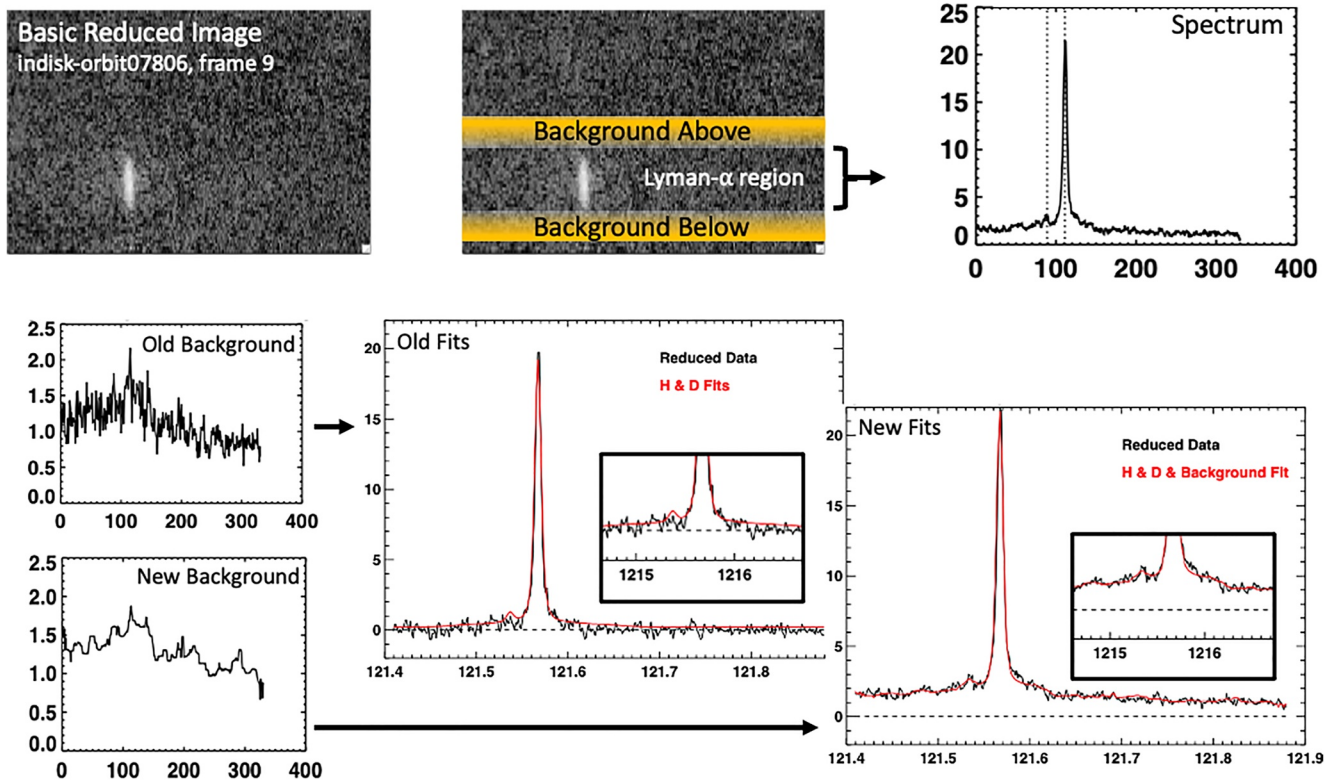


Figure 2. Top Left: A MAVEN/IUVS/Echelle image from frame 9 of 28 total frames in the disk-pointed segment of orbit 7806 (1 October 2018, 15:52:43 UTC). The image is a 29-s exposure and has been reduced by removing the dark signal and filtering out cosmic ray hits and hot pixels (Mayyasi, Clarke, Quémérais, et al., 2017). Top Middle: The Lyman- α region, as well as yellow regions highlighted for deriving the background level are shown. Top Right: The spectrum resulting from integrating the signal across the aperture of the Lyman- α region on the detector. Bottom Left: Two plots showing the background level in the old versus new pipelines where the latter adds a median filter. Bottom Middle: The resulting Lyman- α spectrum (black) derived above the background with the best fit (red). Bottom Right: The resulting Lyman- α spectrum (black) derived with the new background best fits (red). In both the bottom middle and bottom right panels, a horizontal dotted line indicates the zero-signal level, and an insert is shown to zoom-in on the D emission and its fit. In all the spectra and background levels shown, the y-axis represents the signal flux in detected Photons/sec/d λ , where d λ is the wavelength of the pixel element, described further in the text. In the top right and bottom left spectra, the x-axis represents binned pixels in this 384 \times 72 binned image. In the bottom middle and right spectra as well as their inserts, the x-axis represents wavelength in nm.

signal was accounted for by removal of an average background signal, derived from regions on the echelle detector that were physically above and below the regions where the H Lyman- α (121.567 nm) emission is projected onto the detector. The background level was then removed from the Lyman- α region to produce a spectrum that was fit for H and D emissions. This method worked well for the relatively bright H Lyman- α emission but was not conducive to consistently detecting the fainter D Lyman- α emission. Therefore, an alternative method was explored.

The new pipeline determines a background level from the regions above and below the Lyman- α emission region to account for photon scatter in the direction perpendicular to the dispersion. A median filter is then applied to that background level to smooth out any features that may be attributed to photons scattering from the echelle grating in the Lyman- α region in the dispersion direction. The filtered background level is then used as a parameter to fit with the H and D Lyman- α spectra, rather than being subtracted out before fitting H and D emissions. Figure 2 demonstrates the differences in the background level retrieval and compares the resulting fits to the reduced spectrum.

3.3. Cross-Calibration

The HST/STIS data was obtained from Program# 15595 Visit 04 Target Mars-exosphere-STIS observations. The MAVEN/IUVS data were obtained from orbits 08010, 08014, and 08018 (per Table 1) that best matched the HST/STIS observational conditions. The HST data were analyzed using a pipeline developed at Boston University for raw STIS E140H echelle spectra with a long aperture to provide brightness values for the Martian D Lyman- α emission (e.g., Clarke et al., 2004; Quémérais et al., 2009). Since this is an unsupported mode of the STIS

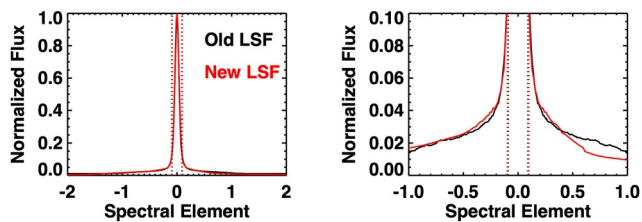


Figure 3. (left) A comparison of the IUVS/Echelle normalized line spread functions. The old LSF (black) is derived from laboratory-generated spectra. The new LSF (red) is derived from in-orbit disk-pointed spectra. (right) The zoomed-in view of the two LSFs are compared to highlight differences in the spectral wings. The dotted vertical lines denote the regions of full-width at half-max for each LSF and overlap for both functions. The functions are normalized to peak values and the x -axis units are in binning-specific spectral element, $d\lambda$, described in the text.

instrument the calibration has also been derived from comparison of observations in other modes of STIS, primarily using G140L and a long aperture.

The optics of an echelle configuration with a cross-dispersion grating provides a two-dimensional spectral format with echelle dispersion in one direction and the cross-dispersion of the echelle orders nearly perpendicular to this (e.g., Howk & Sembach, 2000; Wood et al., 2005; Woodgate et al., 1998). Reduction of the data includes detector dark subtraction, flat fielding of the response, correction for geometric distortion, and then a correction for the angled and curved images to make echelle dispersion linear in one direction and the image of the aperture linear in the other direction. The spectra are then derived by adding rows in the spectral image, and the absolute calibration for sensitivity is derived by comparison of count rates with another calibrated mode (for STIS G140L). The resulting integrated flux observations were compared to derive a new calibration standard for the MAVEN data. When applied to all the observations to date, the updated pipeline and calibration factor resulted in a decrease of $\leq 15\%$ in the fluxes of previously

derived H emission brightness values. This variation is within the overall 20% uncertainty in the calibration (Mayyasi, Clarke, Quémerais, et al., 2017).

3.4. Updating the Line Spread Function and Integration Scheme

Early in the MAVEN mission, the instrument line spread function (LSF) was derived from laboratory data. The in-orbit FUV and Echelle performance was degraded compared with the lab data and so, with MAVEN in orbit, a newer LSF was derived using thousands of Lyman- α emission spectra, measured when the line of sight was disk-pointed. All available disk-pointed observations were used to derive the new LSF in order to average out orbit-to-orbit variations (e.g., illumination conditions, latitude, local time, season, etc.). The resulting LSF shape differed from the theoretical shape only in the wings of the emissions, where the newer LSF showed the signal in those regions to be reduced, as shown in Figure 3. In an echelle spectrum, the same LSF is used to fit both the H and D Lyman- α line emission line shapes and could be used for fitting additional thermal UV emissions detected at Mars with the echelle instrument (e.g., the Oxygen triplet emissions at 130.4 nm and the forbidden O doublet 135.6 nm emissions [Mayyasi et al., 2016]).

In the previous data reduction pipeline, the LSF that best fit the emission line was integrated to within 11 FWHM of the peak and an adjustment factor of 1.13 was used to account for any signal beyond those limits that the physical detector did not capture, as dictated by the binning scheme (Mayyasi, Clarke, Quémerais, et al., 2017). With the newer empirical LSF, the spectral emission flux units were converted to photons/second (Ph/s) using the gain settings of the observations (that varied across the mission [Mayyasi, Clarke, Quémerais, et al., 2017]). The integrated brightness value of the D or H emission was then derived by scaling the peak of the emission by a factor of 0.35541 kR/Ph/s, as determined by the HST comparison, described further in the Cross-Calibration section below. The 1.13 adjustment factor was therefore no longer required.

3.5. Measurement Uncertainty

The newer LSF resulted in updated fits to the background level in the reduced spectrum. The measurement uncertainty in the Lyman- α integrated brightness value is derived from regions that are spectrally far from D and H emissions (Mayyasi, Clarke, Quémerais, et al., 2017). Figure 4 shows the distribution of the uncertainty derived for MAVEN/IUVS echelle observations made between November 2014 and November 2021.

The distribution of measurement uncertainty is near-Gaussian. The old data reduction algorithm resulted in a mean uncertainty of ~ 62 Rayleigh. The new data algorithm results in a mean uncertainty of ~ 59 Rayleigh. In the NASA Planetary Data System (PDS), archived MAVEN/Echelle data products include $1\text{-}\sigma$ uncertainties for both H and D brightness derivations. In several scientific applications of the data that utilized the old data reduction pipeline, conservative $3\text{-}\sigma$ values have been used to depict the measurement uncertainties to account for any detector effects not captured in the data reduction (e.g., Bhattacharyya et al., 2020; Clarke et al., 2017; Mayyasi et al., 2018, 2019, 2020; Mayyasi, Clarke, Bhattacharyya, et al., 2017; Mayyasi, Clarke, Quémerais, et al., 2017).

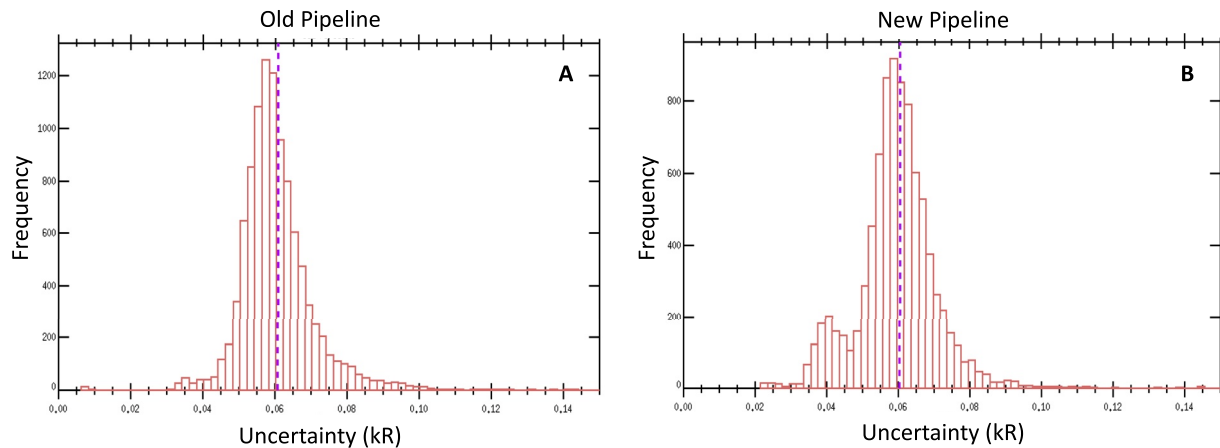


Figure 4. The distribution in the uncertainty derived from the background level in the integrated, reduced spectrum using spectral regions far from D and H Lyman- α emissions (Mayyasi, Clarke, Quémerais, et al., 2017). Panel (a) shows the uncertainties derived with the old data-reduction pipeline. Panel (b) shows the distribution derived with the new data-reduction pipeline. The purple vertical dashed lines show the mean ($1\text{-}\sigma$) value.

4. Results and Discussion

4.1. Comparing Pipeline Brightness Values

The new data reduction pipeline resulted in less-noisy spectra, compared with the previous pipeline. This reduction in background level is attributed to both the improved background level fitting technique as well as to the improved LSF shape. Figure 5 shows a comparison of spectra treated with each of the new and old pipelines for a case where the D Lyman- α emission is considered too faint for a reliable detection. The new data-reduction pipeline fits the H and D emissions on top of the median-filtered background level and uses the new LSF. The old data-reduction pipeline (Figure 5 bottom) removes the background before fitting the H and D emissions to the old LSF.

The old fitting algorithm shows a clear H Lyman- α emission (integrated to ~ 9.9 kR) with a D Lyman- α emission (integrated to 400 R) and a measurement uncertainty (σ , due to residual noise in the spectrum) of 80 R. The uncertainty in the measurement is derived by fitting the signal in the reduced spectrum to the instrument LSF, by incrementally stepping through a wavelength range that is far away from the D and H Lyman- α emission regions (Mayyasi, Clarke, Quémerais, et al., 2017). For the binning scheme of the observation shown in Figure 5, this region is between 121.404 and 121.517 nm. The fits to the residual background level in this wavelength range are averaged to obtain the uncertainty. Compared with the old data reduction pipeline, the improved fitting algorithm for this specific observation results in a brighter H emission (by $\sim 10\%$) and in a fainter D emission (by $\sim 48\%$). The uncertainty in the brightness due to background level with the new fitting algorithm is slightly larger ($\sim 12\%$).

Only D emissions that are above $3\text{-}\sigma$ are considered reliable, as a conservative estimate, as shown in Figure 4. According to the old IUVS Echelle data reduction pipeline, the spectrum shown in Figure 5 would algorithmically (but not visually) yield a D detection.

An example of how a detectable D emission retrieval compares with the old and new data reduction algorithms is shown in Figure 6. The old pipeline shows a clear H Lyman- α emission that integrates to 8.1 kR and a smaller D Lyman- α emission that integrates to 550 R, with an uncertainty for both measurements of 50 R. In the binning scheme of this observation, the uncertainty was derived between 121.277 and 121.370 nm. With the new algorithm, the H brightness in this specific observation is reduced by $\sim 13.7\%$ while the D emission brightness is reduced by $\sim 18\%$. The uncertainty is 20% higher. The results from the newer algorithm fits show a D emission that is well above 3 times the uncertainty and is considered a reliable detection both algorithmically as well as visually.

The updated treatment of background level improved the representation of the empirical fluctuations in the uncertainty, on a frame-by-frame basis, and improved the accuracy of the fits. This resulted in more robust detections

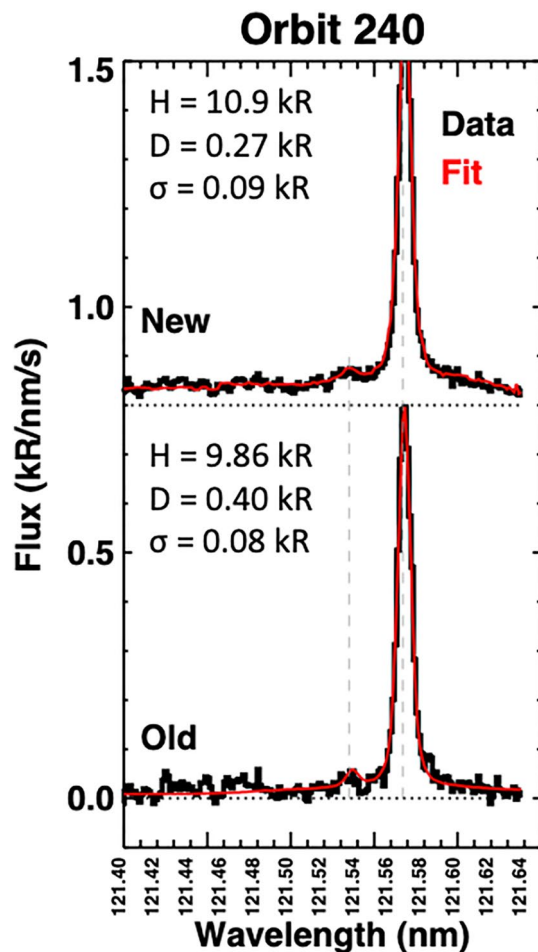


Figure 5. Comparison of new (top) and old (bottom) MAVEN Echelle data reduction pipeline fitting algorithms for on-disk observation of the first frame of orbit 240 (12 November 2014). Data that has been reduced is shown in black and fits to the data are shown in red. The emission line centers of D Lyman- α and H Lyman- α are indicated by the vertical dashed gray lines at 121.535 and 121.567 nm, respectively. A horizontal dotted line indicates the zero-level emission for each spectrum. The top spectrum is offset in vertical coordinates for clarity of comparison and both spectra use the same x-axis range (wavelength in nm). The brightness of each emission, integrated over the aperture, uses the HST calibration and is shown on the left legend. The uncertainty (σ) is derived from a region on the reduced spectrum that is far from the H and D Lyman- α emissions.

The new data reduction algorithm lends more confidence in the integrated emission brightness values for faint D Lyman- α emissions. Specifically, the D emission brightness values will be more reliable, and the associated uncertainties more representative of the background level. This updated data pipeline will be applied to all integrations (individual observations) within an observational scan (that can include anywhere from 8 to over 30 integrations). A full-mission reprocessing of the level1a MAVEN/IUVS/Echelle data will be conducted with this pipeline in order to produce the higher level1c data products on the NASA PDS and will be provided with an upgraded version number to distinguish archived data reduced with the previous pipeline.

4.2. Comparing Low-Res to Hi-Res Brightness Values

The low resolution (low-res) mode of the IUVS instrument, aka FUV mode, measures Lyman- α emissions without the capability of resolving H from D emissions. The FUV mode was calibrated separately using

of fainter emissions (specifically, a 2-fold enhancement in D emission detections) and did not alter the frequency of brighter emission detections (0%).

The differences in H and D emission brightness values when using the new algorithms in data reduction pipeline versus the old in disk-pointed observations, are shown in Figure 7 for orbits spanning 240–15794. These differences demonstrate that the newer algorithm produces trends in the brightness that are similar to the old pipeline results for both D and H. The modifications to the newer data reduction algorithm collectively result in producing slightly fainter H emissions (<15%), and much fainter D emissions (~50%) overall. The uncertainties in the measurements, shown by the vertical bars in the H and D brightness values in Figure 7 are more representative of the background level for the derived emissions.

The algorithm fits negative emission peaks, that occur for D Lyman- α emissions during non-detection cases, where the “peak” at 121.534 nm falls below the zero-level of the background-subtracted reduced spectrum. While negative brightness values are physically implausible, they are expected for faint emission fits and represent retrieval uncertainties that lend statistical significance to the algorithmic fits.

The new data reduction algorithm results in improved fits for faint emissions and successfully reproduces the trends in the reduced brightness as a function of time compared with the older pipeline. To validate this further, the algorithm was applied to the MAVEN/IUVS Echelle data for observations that were not exclusively disk pointed. A comparison of old versus new brightness values is shown in Figure 8 for limb-pointed observations where the tangent point altitude along the instrument line of sight is between 0 and 300 km. This altitude cut-off was chosen to include realistic comparisons of D emissions that become negligible above 300 km of the Martian surface (e.g. Clarke et al., 2017; Mayyasi et al., 2019).

The bottom panels of Figures 7 and 8 show the most significant effect of the improved background correction in the new pipeline for faint D Lyman- α emissions. For on-disk observations, faint emission derivations of brightness values are systematically reduced by ~ 0.12 kR, and off-disk observations of faint emissions are reduced by ~ 0.27 kR, on average. For stronger H Lyman- α emissions, the on-disk brightness derivations are systematically reduced by ~ 0.23 kR, and off-disk observations of H Lyman- α emissions are reduced by ~ 0.67 kR, on average. The off-disk H Lyman- α measurements include an interplanetary H Lyman- α component, discussed further in the next section. In the comparison shown in Figure 8 (top panel), the H brightness derivations are consistent as both pipelines systematically include planetary thermal as well as interplanetary H emissions.

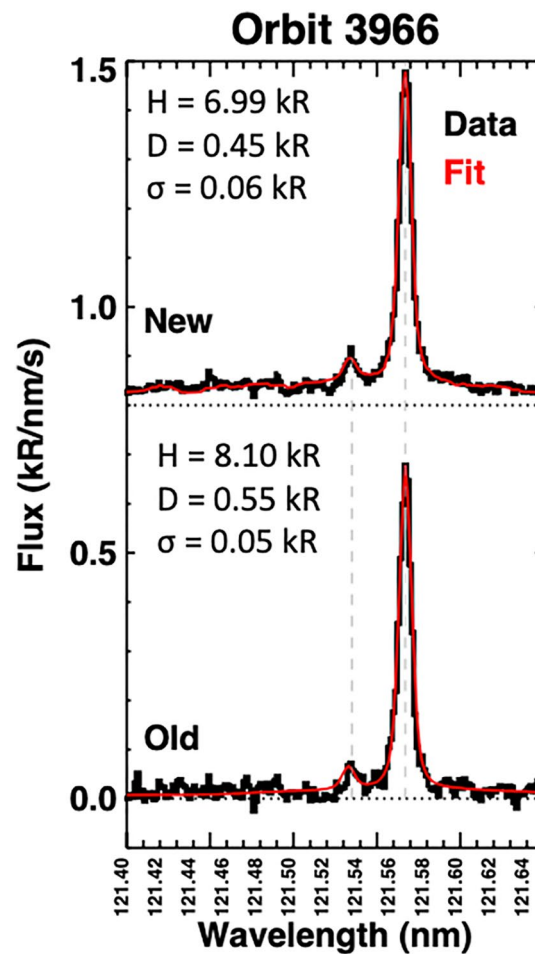


Figure 6. Comparison of new (top) and old (bottom) MAVEN Echelle data reduction pipeline fitting algorithms for on-disk observation of the first frame of orbit 3966 (12 October 2016). Data that has been reduced is shown in black and fits to the data are shown in red. The emission line centers of D Lyman- α and H Lyman- α are indicated by the vertical dashed gray lines at 121.535 and 121.567 nm, respectively. A horizontal dotted line indicates the zero-level emission for each spectrum. The top spectrum is offset in vertical coordinates for clarity of comparison and both spectra use the same x-axis range (wavelength in nm). The brightness of each emission, integrated over the aperture, uses the HST calibration and is shown on the left legend. The uncertainty (σ) is derived from a region on the reduced spectrum that is far from the H and D Lyman- α emissions.

standard stars as well as cross-calibrated with the Echelle mode, aka hi-res mode, early in the MAVEN mission and was found to be consistent within the uncertainties (Chaffin et al., 2018; Mayyasi, Clarke, Quémerais, et al., 2017). To validate the results from the upgraded data reduction pipeline, new brightness values resulting from the ECH mode observations are compared with the brightness values from the FUV mode observations.

Two types of observations are chosen for this comparison: on-disk and off-disk. The on-disk observations are cases where the LOS was pointed at the planetary disk, and where the ECH mode observations included H and D Lyman- α emissions. The brightness values for on-disk observations taken in ECH mode combine the spectrally resolved H and non-negative D contributions for comparison with the low resolution FUV mode observations. The off-disk observations are cases where the LOS was pointed near-upstream of the Inter Planetary Hydrogen (IPH) flow. These observations include H and Doppler shifted IPH Lyman- α emissions. The IPH contribution to the total ECH Lyman- α signal can vary (typically between 0.1 and 1.5 kR) depending on the angle of the instrument line of sight to the IPH flow (e.g., Clarke et al., 1998). The off-disk observations selected for comparison here have a spectrally resolvable IPH contribution. As such, the brightness values for off-disk observations taken in ECH mode combine the spectrally resolved H and IPH contributions for comparison with the low resolution FUV mode observations.

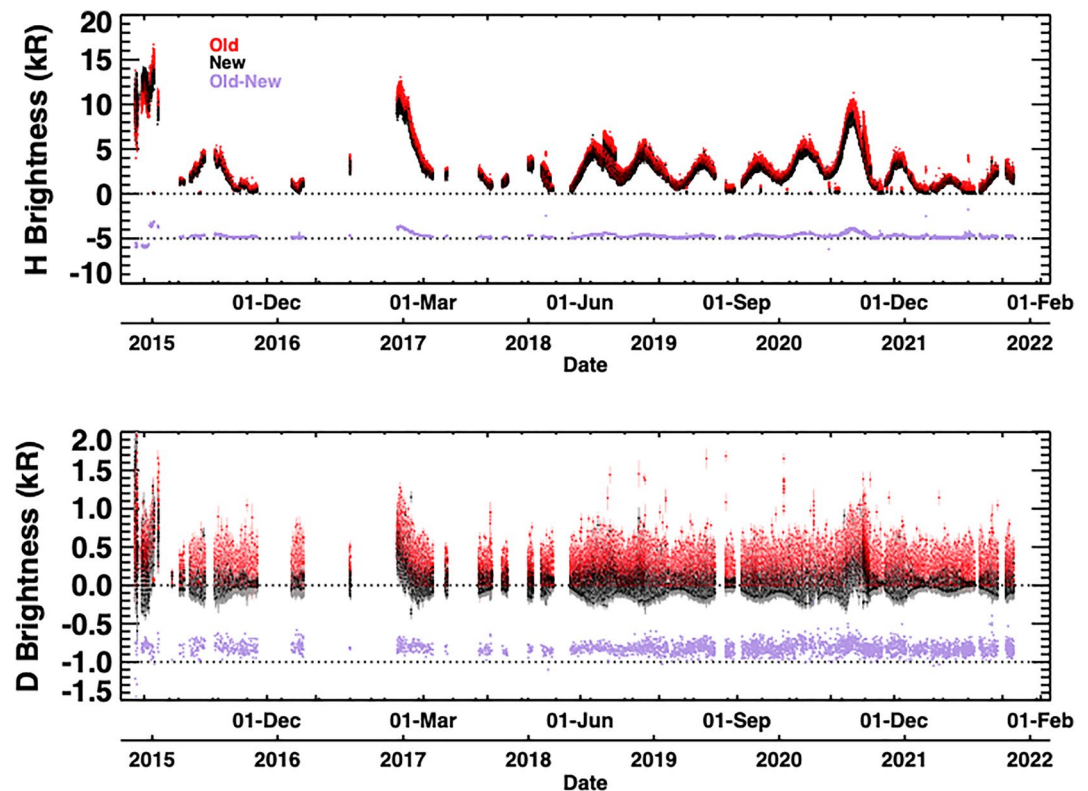


Figure 7. Integrated brightness values for H (top) and D (bottom) Lyman- α emissions for all frames from observations spanning orbits 240–15794 (12 November 2014–14 February 2022) when the IUVS line of sight is pointed at the disk. The old pipeline brightness values are plotted in red; the new values are in black. The differences between the old and new brightness values are shown in purple, offset by -5 and -1 kR for H and D, respectively, for visibility. The $1\text{-}\sigma$ uncertainties in the integrated brightness values are shown as thin vertical lines extending from each data point. The horizontal dotted lines indicate the zero-value brightness levels. Scientific analysis of this data would benefit from co-addition to maximize the signal-to-noise ratio.

The timing and proximity of FUV and Echelle measurements vary for different IUVS observing modes and for different science applications. In Figure 9, a set of near-simultaneous disk-pointed FUV and Echelle measured Lyman- α brightness values are shown that span a range of SZA, Ls, and Mars Years.

The comparison of Lyman- α brightness obtained with the IUVS/ECH and IUVS/FUV was done for observations that were made within 0.2° SZA of each other in on-disk data, and within 2° SZA with the off-disk data. The ECH/FUV brightness ratio showed relatively good agreement. For dayside observations (SZA $< 90^\circ$), the ECH/FUV brightness ratio varied between 0.83 and 1.4, with an average of 1.01. Night-time observations showed more scatter, with an ECH/FUV brightness ratio that varied between 0.56 and 2.7. When all observations are used (SZA ranged between 0° and 162° for this available data set), the ECH/FUV brightness ratio varied between 0.56 and 1.7, with an average of 1.05.

The scatter in the night-time brightness ratio can be explained by the compounded effects of illumination differences, seasons (Ls), and solar activity. The sensitivity of H Lyman- α brightness to ambient conditions is the topic of future work. However, H Lyman- α brightness varies inversely with SZA and small ($\sim 2^\circ$) changes in line of sight illumination can alter the observed brightness (by up to 40%) (Mayyasi et al., 2022). The brightness differences can be further enhanced during the onset of the dusty (perihelion) season at Mars as well as by solar irradiance variations.

The Echelle data shown for MY32 have a SZA range that is on the lower end of the SZA range available from FUV observations in the same orbital range. The Echelle brightness values are therefore on the higher end of the FUV brightness values for this orbital block of orbits. Similarly, the data shown for MY33 has a narrower range for Echelle than for FUV and the former SZA range is on the lower end of the latter. The

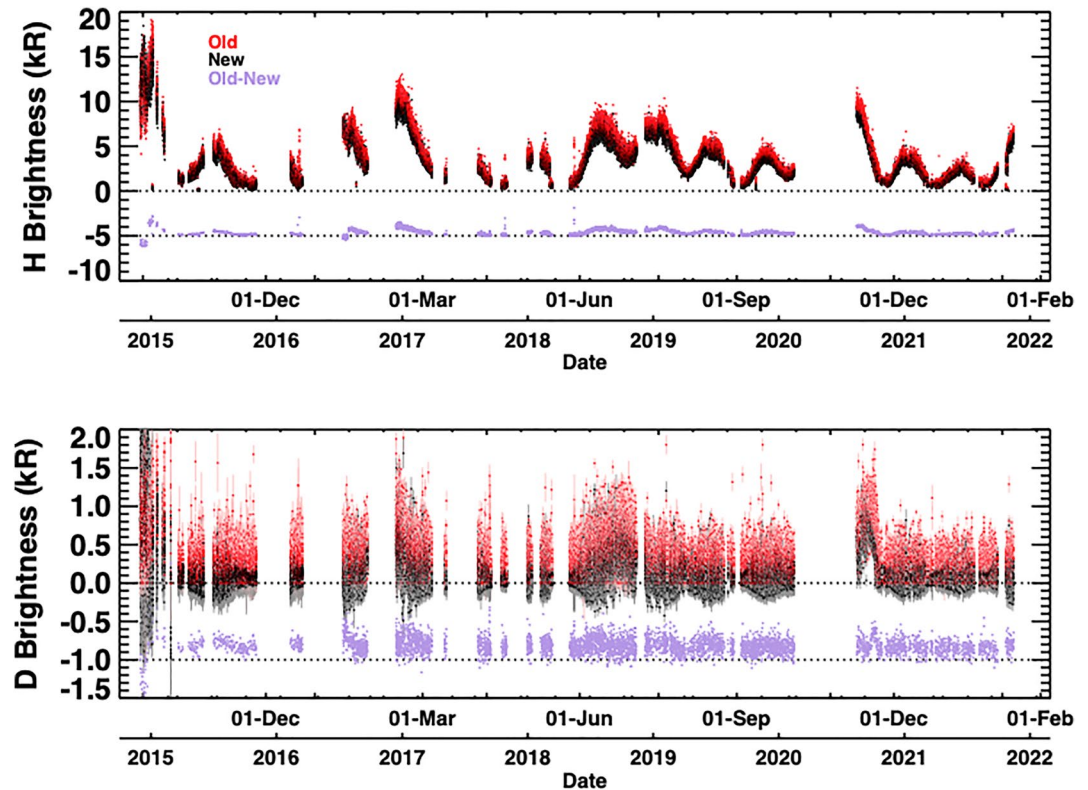


Figure 8. Integrated brightness values for H (top) and D (bottom) Lyman- α emissions from all frames of observations spanning orbits 240–15794 (12 November 2014–14 February 2022) when the IUUV line of sight is pointed at the limb, for observations where the minimum ray height at the tangent point is between the planetary disk and 300 km altitude. The old pipeline brightness values are plotted in red; the new values are in black. The differences between the old and new brightness values are shown in purple, offset by -5 and -1 kR for H and D, respectively, for visibility. The $1\text{-}\sigma$ uncertainties in the integrated brightness values are shown as thin vertical lines extending from each data point. The horizontal dotted lines indicate the zero-value brightness levels. Early mission limb observations have high background levels due to small integration times (1.4 s). Scientific analysis of this data would benefit from co-addition to maximize the signal-to-noise ratio.

brightness values corresponding to this orbital block are consistent with Echelle values on the higher end, as expected. The SZA ranges for the MY34 data block are more closely aligned for both modes, and the resulting brightness values compare similarly. The Echelle data display similar trends in time as the FUV data and are in consistent agreement. When the effects of SZA are binned for each 10° , the FUV and Echelle (ECH) data compare favorably, with difference ranging between 1% and 7% at $\text{SZA} < 90^\circ$ and between 1% and 30% at $\text{SZA} \geq 90^\circ$.

4.3. Implications for Science

This work summarizes a new data reduction pipeline for MAVEN/IUVS Echelle mode data that includes recalibration of the instrument with HST/STIS and includes an improved algorithm for faint-emission fitting. The new data reduction pipeline has been compared with the previous pipeline to show consistency in the results for brightness values and their trends with time while delivering more accurate D Lyman- α emission retrievals.

The algorithms and data comparisons are implemented on a frame-by-frame basis for data collected in each orbit. An IUVS Echelle orbital data product may have 8–20 frames, and an integration time of 1.4–29 s for each frame (Mayyasi, Clarke, Quémerais, et al., 2017). For scientific studies that require D Lyman- α emission derivation and interpretation, individual frames are likely to be co-added in a manner that suits the science implementation in order to further improve the signal-to-noise ratio in observed spectra (e.g., Mayyasi et al., 2019, 2022; Mayyasi, Clarke, Bhattacharyya, et al., 2017).

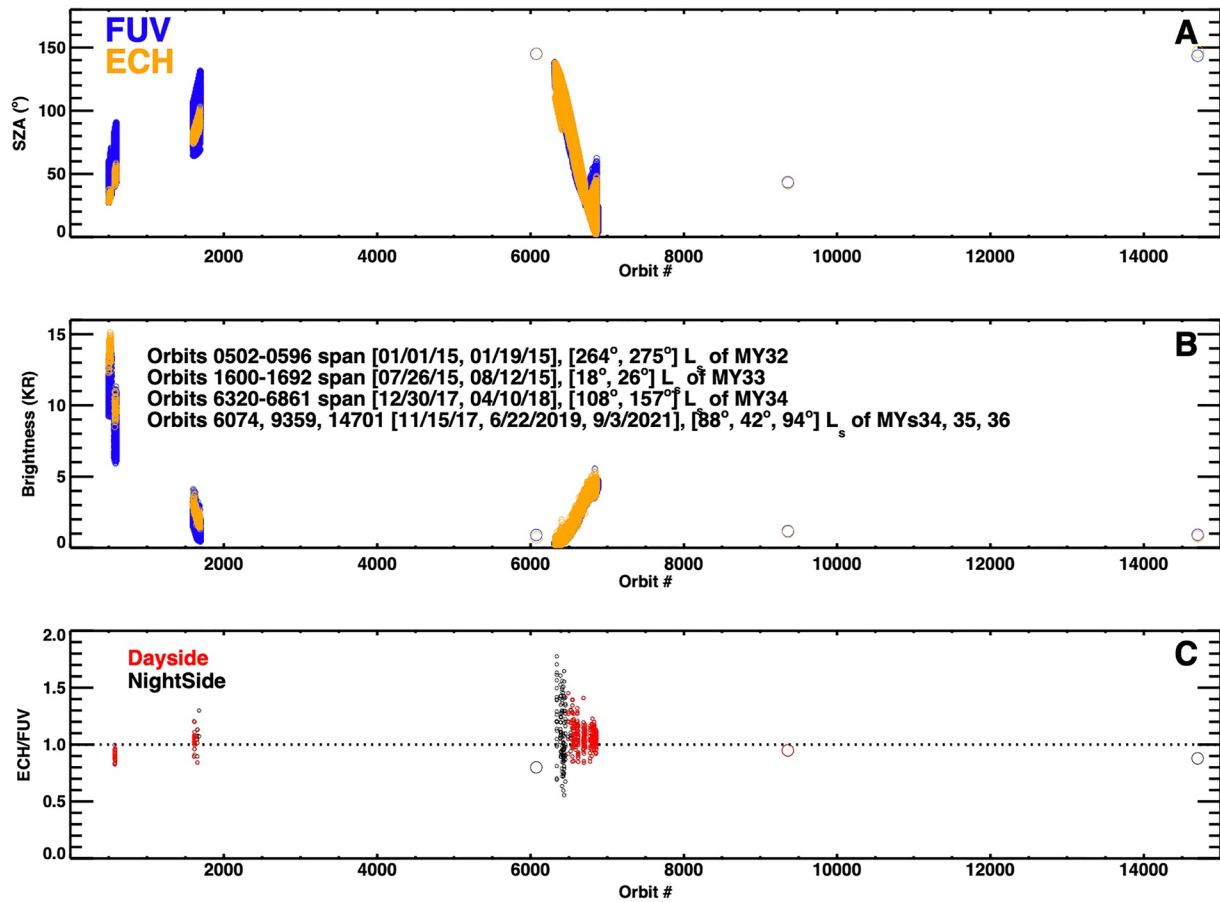


Figure 9. (a) The Solar Zenith Angle of the IUVS instrument line of sight for the low spectral resolution FUV mode (blue) and the high spectral resolution Echelle mode (yellow) for observations that were made close in time. Observations that were pointed at the planetary disk are shown in small circles and observations that were pointed away from the disk are in larger circles. (b) The Lyman- α brightness obtained with the star-calibrated low-resolution FUV mode (blue) and the HST-calibrated high-resolution Echelle mode (yellow). Brightness values of observations that were pointed at the planetary disk (small circles) combine both H and D contributions to compare with the lower resolution FUV data that is unable to resolve the fine line emission difference for each species. Similarly, brightness values of observations that were pointed away from the planetary disk (larger circles) combine both H and IPH contributions in the ECH mode to compare with FUV mode values. The data ranges (for on-disk observations) and individual orbits (for off-disk observations) span different Martian seasons across four Mars Years (MY). (c) The ratio of ECH to FUV brightness made for observations that were closest in time and SZA. The data observed at daytime conditions (SZA < 90°) are shown in red. Data observed at night-time conditions (SZA ≥ 90°) are shown in black.

The implications of this work for science are demonstrated in Figure 10. The previous data reduction pipeline yielded D Lyman- α emission detections that were not consistent with visually inspected spectra and so, data analyses were limited to seasonal times when the D Lyman- α emission was at its brightest (~210°–310° L_s) (Mayyasi et al., 2019; Mayyasi, Clarke, Bhattacharyya, et al., 2017). The new data reduction pipeline results in more accurate faint emission retrievals for D Lyman- α that are consistent with visual inspection. As a result, the D Lyman- α emissions can be more reliably obtained for a wider seasonal range (e.g., ~120°–360° L_s in MY34). The improvements described in this work more than double the faint-emission data set that would be suited for scientific analysis.

Determining the D Lyman- α emission brightness at these seasonal times allows for improved interpretations of water loss from Mars. The lower atmospheric circulation patterns and responses to seasonal drivers occur year-round. The D and H Lyman- α emissions can be combined with radiative transfer models to derive densities and the D/H ratio in the upper atmosphere of Mars. These data may also be used to derive escape rates and escape fluxes of water-originating atoms. The derived properties may be used to infer estimates of water isotopic fractionation and to derive more accurate estimates of Mars' primordial water content and loss over time (e.g., Cangi et al., 2020; Jakosky, 2021; Mayyasi et al., 2022).

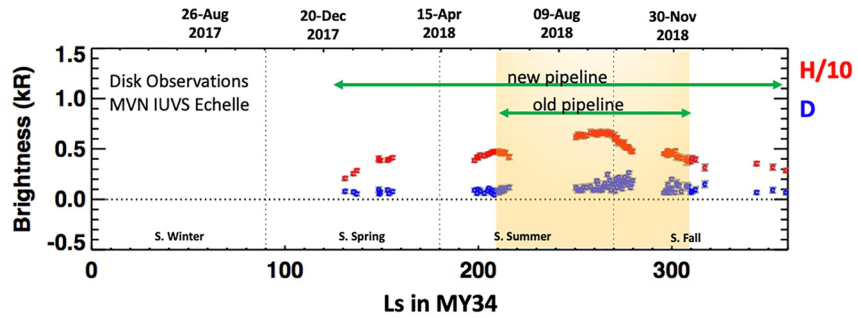


Figure 10. The new on-disk derived Lyman- α brightness values versus solar longitude (Ls) for D (blue) and H (red, divided by 10 to facilitate comparison) emissions obtained with MAVEN/IUVS/Echelle in Mars Year 34 (5 May 2017–23 March 2019). The yellow shaded region indicates the seasonal range where D emission brightness values were considered reliable, as derived with the old pipeline. The upgraded pipeline produces a broader range (all plotted values) of reliable D detections and facilitates improved science interpretations.

Data Availability Statement

The MAVEN data used in this study are available on the NASA PDS Atmospheres Node at: https://pds-atmospheres.nmsu.edu/data_and_services/atmospheres_data/MAVEN/maven_main.html. IUVS echelle level1a and level1c v13 data were used. At the time of this writing, the MAVEN/IUVS/Echelle PDS data are generated using the old pipeline and cover mission observations through delivery #31, MAVEN orbit 17004, 15 August 2022. A full mission reprocessing of IUVS data products, including updates to the ECH pipeline described here, are presently underway. The resulting level1a and level1c v14 data are targeted for public access in the next 3–6 months. The HST data used in this study are available on the MAST archive at: <https://archive.stsci.edu/hst/>.

Acknowledgments

The authors would like to thank two anonymous reviewers for their careful read of the manuscript and for their constructive suggestions that have improved the delivery of this work. This work was funded, in part, by NASA contract #1000320450 from the University of Colorado to Boston University, and Space Telescope Science Institute (STScI) Grant DD-15595 to Boston University.

References

- Anderson, D. E., & Hord, C. W. (1971). Mariner 6 and 7 ultraviolet spectrometer experiment: Analysis of hydrogen Lyman-alpha data. *Journal of Geophysical Research*, 76(28), 6666–6673. <https://doi.org/10.1029/ja076i028p06666>
- Ben Jaffel, L., Kim, Y. J., & Clarke, J. T. (2007). The H Lyman- α emission line from the upper atmosphere of Jupiter: Parametric radiative transfer study and comparison with data. *Icarus*, 190(2), 504–527. <https://doi.org/10.1016/j.icarus.2007.03.013>
- Bertaux, J. L., Korabiev, O., Perrier, S., Quémérais, E., Montmessin, F., Leblanc, F., et al. (2006). SPICAM on Mars Express: Observing modes and overview of UV spectrometer data and scientific results. *Journal of Geophysical Research*, 111(E10), E10S90. <https://doi.org/10.1029/2006JE002690>
- Bhattacharyya, D., Chaufray, J.-Y., Mayyasi, M., Clarke, J., Stone, S., Yelle, R., et al. (2020). Two-dimensional model for the Martian exosphere: Applications to hydrogen and deuterium Lyman α observations. *Icarus*, 339, 113573. <https://doi.org/10.1016/j.icarus.2019.113573>
- Bhattacharyya, D., Clarke, J. T., Bertaux, J.-L., Chaufray, J.-Y., & Mayyasi, M. (2015). A strong seasonal dependence in the Martian hydrogen exosphere. *Geophysical Research Letters*, 42(20), 8678–8685. <https://doi.org/10.1002/2015GL065804>
- Bohlin, R., Deustua, S., & de Rosa, G. (2019). Hubble Space Telescope Flux Calibration. I. STIS and CALSPEC. *The Astronomical Journal*, 158(5), 211. <https://doi.org/10.3847/1538-3881/ab480c>
- Cangi, E., Chaffin, M., & Deighan, J. (2020). Higher Martian atmospheric temperatures at all altitudes increase the D/H fractionation factor and water loss. *Journal of Geophysical Research*, 125, 12. <https://doi.org/10.1029/2020JE006626>
- Chaffin, M. S., Chaufray, J. Y., Deighan, D., Schneider, N. M., Mayyasi, M., Clarke, J. T., et al. (2018). Mars H escape rates derived from MAVEN/IUVS Lyman alpha brightness measurements and their dependence on model assumptions. *Journal of Geophysical Research: Planets*, 123(8), 2192–2210. <https://doi.org/10.1029/2018JE005574>
- Chaffin, M. S., Chaufray, J. Y., Deighan, J., Schneider, N. M., McClintock, W. E., Stewart, A. I. F., et al. (2015). Three-dimensional structure in the Mars H corona revealed by IUVS on MAVEN. *Geophysical Research Letters*, 42(21), 9001–9008. <https://doi.org/10.1002/2015GL065287>
- Chaffin, M. S., Chaufray, J.-Y., Stewart, I., Montmessin, F., Schneider, N. M., & Bertaux, J.-L. (2014). Unexpected variability of Martian hydrogen escape. *Geophysical Research Letters*, 41(2), 314–320. <https://doi.org/10.1002/2013GL058578>
- Chamberlain, J. (1963). Planetary coronae and atmospheric evaporation. *Planetary and Space Science*, 11(8), 901–960. [https://doi.org/10.1016/0032-0633\(63\)90122-3](https://doi.org/10.1016/0032-0633(63)90122-3)
- Chaufray, J.-Y., Gladstone, G. R., Waite, J. H., & Clarke, J. T. (2010). Asymmetry in the Jovian auroral Lyman- α line profile due to thermospheric high speed flow. *Journal of Geophysical Research*, 115(E5), E05002. <https://doi.org/10.1029/2009JE003439>
- Clarke, J., Bertaux, J.-L., Owen, T., & Nagy, A. (2004). HST/STIS observations of the extended Martian upper atmosphere. In *AAS DPS Meeting #36, Id.47.02* (Vol. 36, p. 1182).
- Clarke, J., Lalletment, R., Bertaux, J.-L., Fahr, H., Quémérais, E., & Scherer, H. (1998). HST/GHRS observations of the velocity structure of interplanetary hydrogen. *Acta Pathologica Japonica*, 49(1), 485–488. <https://doi.org/10.1086/305628>
- Clarke, J., Mayyasi, M., Bhattacharyya, D., Schneider, N., Chaufray, J.-Y., Bertaux, J.-L., et al. (2019). The D/H ratio in the Martian upper atmosphere. In *EPSC Abstract* (Vol. 13), EPSC-DPS2019-868-1.
- Clarke, J. T., Bertaux, J.-L., Chaufray, J.-Y., Gladstone, G. R., Quémérais, E., Wilson, J. K., & Bhattacharyya, D. (2014). A rapid decrease of the hydrogen corona of Mars. *Geophysical Research Letters*, 41(22), 8013–8020. <https://doi.org/10.1002/2014GL061803>

- Clarke, J. T., Mayyasi, M., Bhattacharyya, D., Schneider, N. M., McClintock, W. E., Deighan, J. I., et al. (2017). Variability of D and H in the Martian upper atmosphere observed with the MAVEN IUVS echelle channel. *Journal of Geophysical Research: Space Physics*, 122(2), 2336–2344. <https://doi.org/10.1002/2016JA023479>
- Howk, J., & Sembach, K. (2000). Background and scattered-light subtraction in the high-resolution Echelle modes of the Space Telescope Imaging Spectrograph. *Acta Pathologica Japonica*, 119(5), 2481–2497. <https://doi.org/10.1086/301354>
- Jakosky, B. (2021). Atmospheric loss to space and the history of water on Mars. *Annual Review of Earth and Planetary Sciences*, 49(1), 71–93. <https://doi.org/10.1146/annurev-earth-062420-052845>
- Jakosky, B. M., Lin, R. P., Grebowsky, J. M., Luhmann, J. G., Mitchell, D. F., Beutelschies, G., et al. (2015). The Mars atmosphere and volatile evolution (MAVEN) mission. *Space Science Reviews*, 195(1–4), 3–48. <https://doi.org/10.1007/s11214-015-0139-x>
- Mayyasi, M., Bhattacharyya, D., Clarke, J., Catalano, A., Benna, M., Mahaffy, P., et al. (2018). Significant space weather impact on the escape of hydrogen from Mars. *Geophysical Research Letters*, 45(17), 8844–8852. <https://doi.org/10.1029/2018GL077727>
- Mayyasi, M., Clarke, J., Bhattacharyya, D., Chaufray, J. Y., Benna, M., Mahaffy, P., et al. (2019). Seasonal variability of deuterium in the upper atmosphere of Mars. *Journal of Geophysical Research: Space Physics*, 124(3), 2152–2164. <https://doi.org/10.1029/2018JA026244>
- Mayyasi, M., Clarke, J., Bhattacharyya, D., Deighan, J., Jain, S., Chaffin, M., et al. (2017). The variability of atmospheric deuterium brightness at Mars: Evidence for seasonal dependence. *Journal of Geophysical Research: Space Physics*, 122(10), 10811–10823. <https://doi.org/10.1002/2017JA024666>
- Mayyasi, M., Clarke, J., Chaufray, J.-Y., Kass, D., Bougher, S., Bhattacharyya, D., et al. (2022). Solar cycle and seasonal variability of H in the upper atmosphere of Mars. *Icarus*, 115293. <https://doi.org/10.1016/j.icarus.2022.115293>
- Mayyasi, M., Clarke, J., Combi, M., Fougere, N., Quémérais, E., Katushkina, O., et al. (2020). Ly α observations of Comet C/2013 A1 (siding spring) using MAVEN IUVS Echelle. *Acta Pathologica Japonica*, 160(1), 10. <https://doi.org/10.3847/1538-3881/ab8f96>
- Mayyasi, M., Clarke, J., Quémérais, E., Katushkina, O., Bhattacharyya, D., Chaufray, J. Y., et al. (2017). IUVS echelle-mode observations of interplanetary hydrogen: Standard for calibration and reference for cavity variations between Earth and Mars during MAVEN cruise. *Journal of Geophysical Research: Space Physics*, 122(2), 2089–2105. <https://doi.org/10.1002/2016JA023466>
- Mayyasi, M., Clarke, J., Stewart, I., McClintock, W., Schneider, N., Jakosky, B., et al. (2016). Oxygen emission line properties from the analysis of MAVEN-IUVS Echellograms of the Martian atmosphere. In *DPS meeting* (Vol. 48). American Astronomical Society. id.220.02.
- McClintock, W., Schneider, N. M., Holsclaw, G. M., Clarke, J. T., Hoskins, A. C., Stewart, I., et al. (2014). The imaging ultraviolet spectrograph (IUVS) for the MAVEN mission. *Space Science Reviews*, 195(1–4), 75–124. <https://doi.org/10.1007/s11214-014-0098-7>
- Quémérais, E., Lallement, R., Bertaux, J.-L., Koutroumpa, D., Clarke, J. T., Kyrola, E., & Schmidt, W. (2006). Interplanetary Lyman α line profiles: Variations during solar activity cycle. *Astronomy & Astrophysics*, 455(3), 1135–1142. <https://doi.org/10.1051/0004-6361:20065169>
- Quémérais, E., Lallement, R., Sandel, B., & Clarke, J. T. (2009). Interplanetary Lyman α observations: Intensities from voyagers and line profiles from HST/STIS. *Space Science Reviews*, 143(1–4), 151–162. <https://doi.org/10.1007/s11214-008-9379-3>
- Sohn, S. T., Boestrom, K. A., & Proffitt, C. (2019). “STIS data Handbook”, version 7.0. STIScl.
- Wood, B., Redfield, S., Linsky, J., Müller, H.-R., & Zank, G. (2005). Stellar Lyman α emission lines in the Hubble Space Telescope Archive: Intrinsic line fluxes and absorption from the heliosphere and astrospheres. *Acta Pathologica Japonica*, 159(1), 118–140. <https://doi.org/10.1086/430523>
- Woodgate, B., Kimble, R. A., Bowers, C. W., Kraemer, S., Kaiser, M. E., Danks, A. C., et al. (1998). The space telescope imaging spectrograph design. *Publications of the Astronomical Society of the Pacific*, 110(752), 1183–1204. <https://doi.org/10.1086/316243>